Full-field correlation-based image processing for PIV

H. Nobach, N. T. Ouellette, E. Bodenschatz and C. Tropea

Abstract Due to its high robustness, correlation-based particle image velocimetry (PIV) has become the prime choice for processing image-based flow measurements in fluid dynamics experiments. However, in recent years, whole-field techniques like optical flow methods have been successfully applied to these kind of images. To avoid the dependence of optical flow methods on intensity variations and to combine the robustness of the correlation-based PIV technique with the whole-field flow description of the optical flow method, a hybrid estimation procedure has been developed. It is an iterative method, optimizing a dense, hypothetical velocity field with respect to vanishing residual displacements, obtained by image correlation.

1

Introduction

Particle image velocimetry (PIV), which utilizes the correlation of image sub-spaces for local displacement estimation, has been found to be a robust and easy to use image processing method for experimental fluid dynamics. The high seeding density and statistical character of PIV make it insensitive to the in-plane or out-of-plane particle loss or intensity variation that influence methods like particle tracking velocimetry detrimentally. The main drawback of PIV processing is the evident compromise between achievable spatial resolution and the probability of fault estimates (outliers), determined primarily by the chosen size of the interrogation areas.

To reduce the probability of outliers, which leads to higher spatial resolution, even for small interrogation areas, the information from neighboring areas must be considered. In state of the art PIV procedures, this is realized by validation steps that follow each displacement estimate, in combination with coarse to fine multi-grid and iterative algorithms with window shifts and deformation (Scarano, 2002).

During the past few years, new processing methods have been developed based on whole-field descriptions of the observed flow. In these cases a dense, hypothetical velocity field is optimized iteratively until two consecutive measured images can be transformed by the hypothetical field. The main advantages of this are the automatically fulfilled neighbor constraint and the possibility of implementing physical models of the flow. Appropriate algorithms have been realized evaluating the optical flow (Ruhnau et al. , 2005). This technique was found to be sensitive to the intensity fluctuations of single particles and whole field illumination as well as to the presence of background features. Hybrid methods that combine a densely sampled hypothetical velocity field and correlation-based displacement estimation are superior. An example of such a method, including a physics-based dynamic model, has been implemented and applied by Okuno et al. (2000). Unfortunately, the high numerical costs make an appropriate implementation of the variation and optimization of the hypothetical velocity field in combination with the calculation of remaining local correlations infeasible.

To overcome this limitation, an alternative method is presented here. It utilizes a densely sampled hypothetical velocity field to derive appropriately deformed images that, ideally, match each other. The hypothetical velocity field is optimized iteratively towards a minimum difference of the image content, which is similar to optical flow. Instead of the transformation and the comparison of image intensities, however, the correlation between images is

H. Nobach[1,2], N. T. Ouellette[1], E. Bodenschatz[1,2] and C. Tropea[3]

[1]Laboratory of Atomic and Solid State Physics, Cornell University, Clark Hall of Science Ithaca NY, USA
[2]Max-Planck-Institut für Dynamik und Selbstorganisation, Bunsenstr. 10, 37073 Göttingen
[3]Fachgebiet Strömungslehre und Aerodynamik, Technische Universität Darmstadt, Darmstadt, Germany

Correspondence to:
Dr.-Ing. Holger Nobach, LASSP, Cornell University, 616 Clark Hall of Science, Ithaca NY 14853-2501, USA, E-mail: holger.nobach@nambis.de
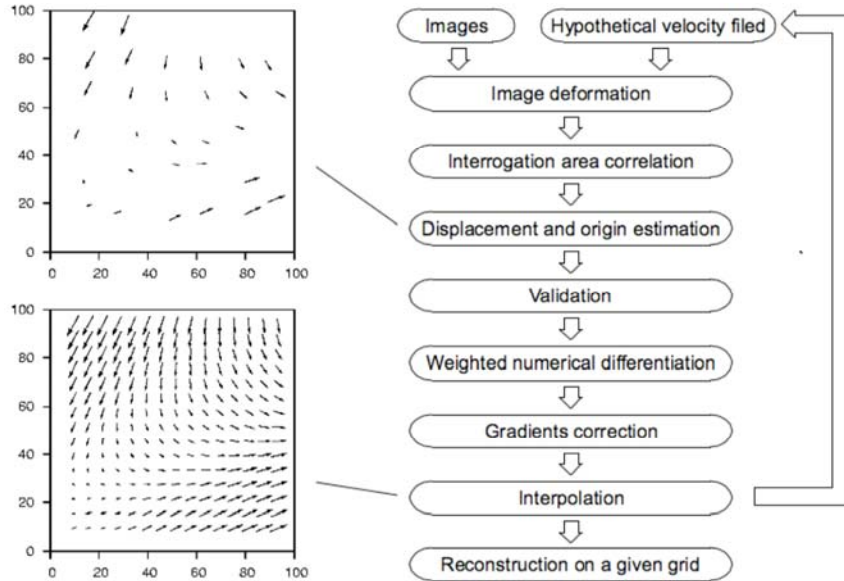
Fig. 1: Overview of the full-field, correlation-based PIV image processing

used. A vanishing residual displacement obtained by image correlation is the figure of merit. To reduce the numerical costs compared to the trial-and-error method of Okuno et al. (2000), our method employs the calculated correlation functions to derive local velocities that are then used to correct the hypothetical velocity field directly. Therefore, the entire algorithm is comparable to iterative window shift and deformation or image deformation techniques with sub-pixel resolution (Huang et al. , 1993; Jambunathan et al. , 1995; Tokumaru and Dimotakis, 1995; Lecordier, 1997; Fincham and Delerce, 2000; Scarano and Riethmuller, 2000; Gui and Wereley, 2002) where the correlation is calculated from square interrogation windows which are re-sampled from the measured images, whereas the window deformation and image re-sampling realizes local offsets for each pixel based on the dense hypothetical and full velocity field. Several improvements have been implemented regarding the image re-sampling, correlation, maximum location, numerical differentiation and velocity interpolation, which are described in detail in the following section.

2
Estimation Procedure

The entire algorithm is a multi-step correction loop of the hypothetical velocity field. Fig. 1 gives an overview of the algorithm. The hypothetical velocity field with components $u(x;y)$ and $v(x;y)$ corresponds to the actual estimate of the procedure, which is improved iteratively. This velocity field is sampled densely, so that for each pixel in the image a local velocity can be obtained.

2.1
Image Deformation

The entire image is deformed according to the hypothetical velocity field by utilizing a symmetric shift of each pixel with indices $(i;j)$ at the co-ordinates $(x_i;y_j)$ by $\pm u(x;y)/2$ and $\pm v(x;y)/2$. The gray values of the deformed images are obtained from the original images by re-sampling at the positions $(x_r;y_r)$ with

$$x_r(x_i;y_j) = x \pm u(x_i;y_j)/2 \quad \text{and} \quad y_r(x_i;y_j) = y \pm v(x_i;y_j)/2, \tag{1}$$

(minus sign for the first image and plus sign for the second). In general, the resampled positions are not integers. Therefore, image interpolation must be used. Since this is the most crucial step of the procedure in terms of the achievable accuracy, a high-precision sub-pixel interpolation based on a Gaussian low-pass filter is used (Nobach et al. , 2005), here with an 11×11 kernel. The filter coefficients are given by
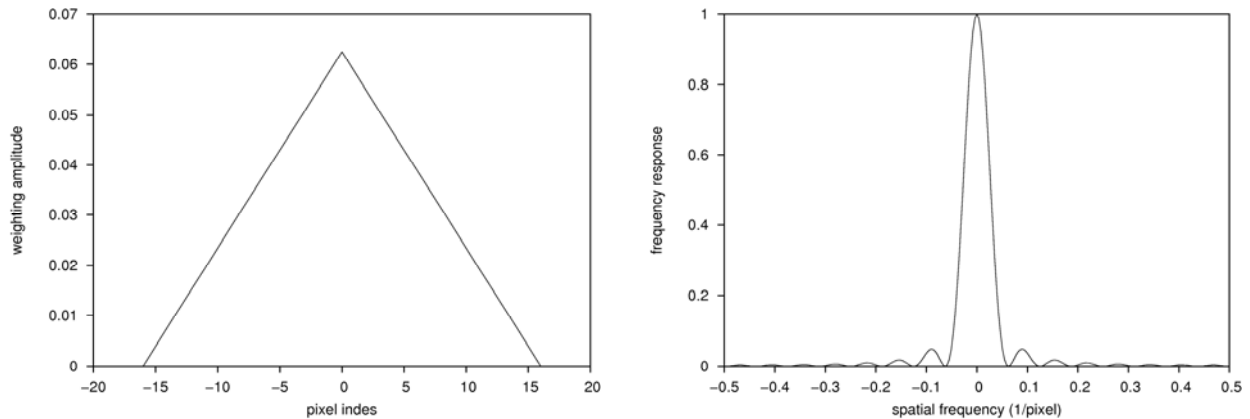
Fig. 2: Triangular weighting function and its frequency response

$$c_{ij}(x_r; y_r) = \exp\left\{-b\left[(x_r - x_i)^2 + (y_r - y_j)^2\right]\right\} \tag{2}$$

with the indices $(i;j)$ of the original images pixels and their appropriate co-ordinates $(x_i;y_j)$. A coefficient $b = 0.5$ has been found to be optimal in terms of achievable accuracy and insensitivity to noise.

2.2

Interrogation Area Correlation

Since entire images are deformed according to the hypothetical velocity field, the deformed images coincide if the hypothetical velocity field exactly represents the particle displacements. The idea of the procedure is to locally correct small residual displacements for a non-optimal hypothetical velocity field, where the local displacements are obtained by correlating arbitrary interrogation areas of the deformed images. In general, the local correlation and the residual displacement can be calculated for each individual pixel. To reduce the numerical costs, interrogation areas and correlation planes are calculated on a single grid only, corresponding to the chosen final grid of the resulting vector map. Since entire images have been deformed and re-sampled in the previous step, no more interpolation is necessary and the interrogation areas to be correlated are obtained simply by truncating the deformed images.

The two interrogation areas with their gray values $z_1(i;j)$ and $z_2(i;j)$ are then correlated using a simple FFT routine. This introduces additional errors due to the inherent wrap-around error of the FFT and due to truncated particles at the borders of the interrogation areas (Nogueira et al. , 2001; Nobach, 2004). These errors can be avoided by a normalized correlation function such as that due to Ronneberger et al. (1998). However, since these errors vanish for a zero displacement, which is asymptotically achieved by our algorithm, the simple FFT routine is acceptable and reduces computational costs.

To improve the algorithm, two weighting functions have been implemented:

- **Image Weighting:** The image interpolation algorithm (Sec. 2.1) with its large 11×11 Gaussian low-pass filter kernel introduces systematic deviation at the image borders, since no gray values are available from outside the original image bounds. Therefore, individual weights are used, which correspond to the reliability of each individual pixel (Nobach et al. , 2005). In the present study, this value is obtained as the summation of the filter coefficients in Eq. (2), corresponding to pixels inside the bounds of the original images. This weighting scheme can also be utilized to mask certain regions of the images. Note that these weighting factors $w_1(i;j)$ and $w_2(i;j)$ belong to the individual pixels of the deformed images and can be different for the two images.

- **Interrogation Area Weighting:** The local correction of the residual displacements requires a high spatial resolution for the displacement estimation. To increase the spatial resolution of the correlation-based displacement estimation a weighting scheme is applied to the interrogation areas (Nogueira et al. , 1999). To encourage discussion about the optimal weighting scheme, an alternative function is
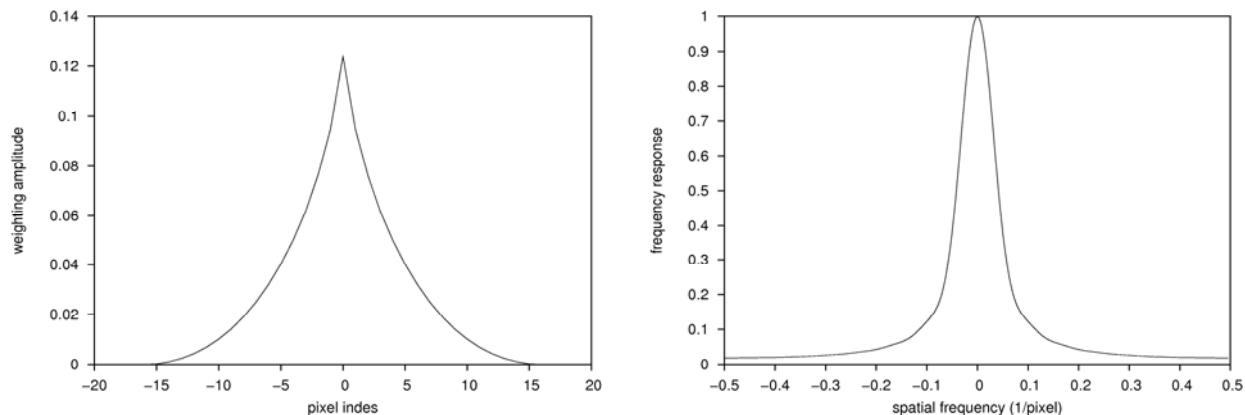
Fig. 3: Superimposed triangular weighting functions and the frequency response
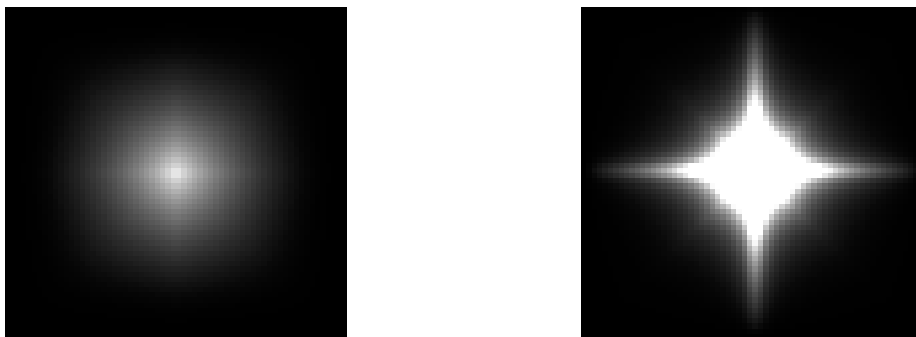

Fig. 4: Two-dimensional weighting function (left) and its frequency response (right; zero frequency in the center of the image)

introduced here. The main requirement for the weighting function is a positive frequency response in the whole frequency range.

Since the frequency response of a triangular window function is non-negative in the whole frequency range (Fig. 2), this simple function is a suitable starting point to derive a proper weighting function. To avoid the zero values of the frequency response, another triangular weighting function could be superimposed, which has its zero values at those frequencies where the first triangular weighting function has positive values and vice versa. However, another figure of merit for the optimality of the weighting function is the amount of information used. Since a wider weighting function corresponds to more information used, wider weighting functions yield more stable displacement estimates. Unfortunately, this corresponds to a narrow spectral peak, which damps high-frequency fluctuations. A practical compromise is given by the superposition of all triangular functions that are narrower than one dimension of the interrogation area. This superposition, normalized to have a unity integral can be expressed explicitly as

$$w_{\mathrm{IA}}(x) = \frac{4}{W} - \frac{8|x|}{W^2}\left(1 + \ln\frac{W}{2} - \ln|x|\right) \tag{3}$$

where W is the width of the interrogation window. Fig. 3 shows the appropriate weighting function for $W = 32$ and its frequency response, which is positive in the whole frequency range. Applying the same weighting function in the y direction and shifting the window function to the center of the interrogation area yields the two-dimensional weighting image $w_{\mathrm{IA}}(i;j)$ shown in Fig. 4 together with its frequency response.
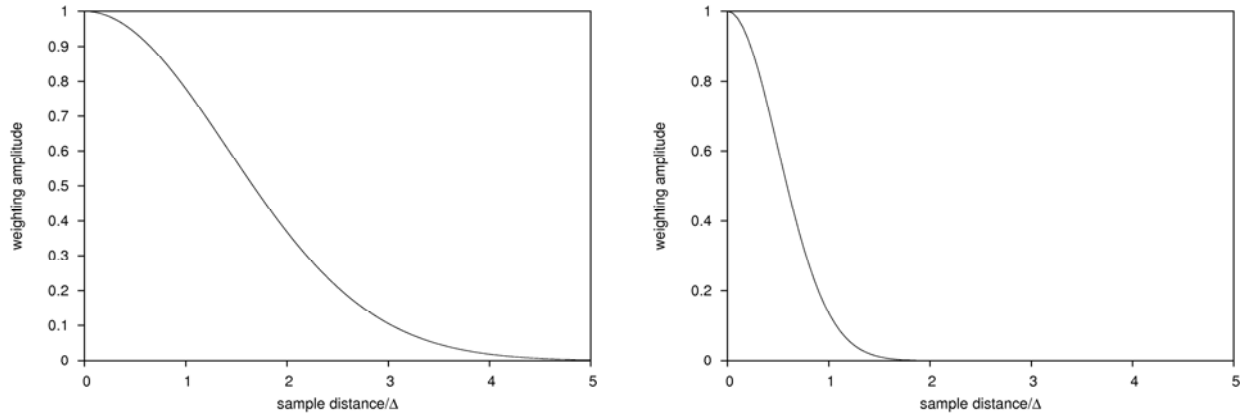
Fig. 5: Weighting functions for the numerical differentiation (left) and the velocity interpolation (right)

Since systematic errors vanish for the asymptotically achieved zero displacement, both weighting schemes can be applied to the image gray values by simple multiplication, yielding the two functions

$$z_1(i; j)w_1(i; j)w_{IA}(i; j) \quad \text{and} \quad z_2(i; j)w_2(i; j)w_{IA}(i; j), \tag{4}$$

that are then correlated by the FFT routine.

2.3
Displacement and Origin Estimation

The mean particle displacement inside the interrogation area is calculated from the maximum of the correlation plane and its neighboring values by a sub-pixel regression. In the present study an explicit solution of the regression of a two-dimensional second-order polynomial to the logarithms of the nine points around the maximum is used (Nobach and Honkanen, 2005). Due to the irregular sampling of the images by tracer particles, the information about the displacement field is only locally available. In the case of velocity gradients this introduces errors by assigning the velocity estimate to the center of the interrogation window. Higher accuracy can be achieved by estimating the effective origin directly from the images. Willert (2000) introduced the idea of relocating the origin to the center of mass using the image intensities. Lindken et al. (2003) and Young et al. (2004) introduced more reliable realizations of this idea using the center of mass, highest intensity, or pixel-wise product of the images shifted by the obtained displacement. An alternative procedure that yields results equivalent to those of Lindken et al. (2003), has been introduced by Nobach and Tropea (2005). It utilizes FFT routines similar to the displacement estimation procedure.

As a result the velocity vector map is irregularly sampled as indicated in Fig. 1 and the velocities must be re-mapped to a given, regular grid. However, the location of the individual velocity vectors is more accurate.

2.4
Validation

Due to the noise in the images and other disturbing influences, validation of the computed displacements and their origins is recommended. Validation procedures based on the increased correlation of the two deformed images after a successful correction loop have been found to be reliable, which can be completed by outlier detection based on the statistics of the obtained velocity estimates. However, since only simulated images are considered in the following performance test, the validation step has not been used in this study.

2.5

Weighted Numerical Differentiation

Since simple interpolation of the velocity values, such as linear interpolation or averaging, preferably weighted by a function of the distance to the obtained velocity origins, suppresses the dynamic bandwidth of the velocity field, an alternative interpolation of the velocity field is given in the next sections. This interpolation scheme uses additional information from the velocity gradients. Therefore, the irregularly sampled and validated velocity vector field is completed by velocity gradient estimates computed by numerical differentiation.

In principle, the velocity gradients at a certain position ($x;y$) can be obtained by two-dimensional linear regressions of the two velocity components u_k and v_k from the neighboring velocity samples at their origins ($x_k;y_k$). Unfortunately, values which are too far away from the investigated position cannot follow the velocity dynamics and do not sufficiently represent the velocity gradient at this position. On the other hand, using only samples that are very close to the investigated position leads to a large uncertainty in the gradient estimates (small difference of relatively high values). Therefore, all available velocity samples should be used for the regression procedure, applying a certain weighting function $w_D(x_k–x;y_k–y)$ that weights samples within a certain distance of the investigated location more heavily.

In this study a Gaussian weighting function has been used. The optimal width of the weighting function depends on the given density of velocity samples, since direct neighbors of a certain velocity sample are preferable for calculation of this sample's velocity gradients. For a given offset between interrogation areas Δ, the weighting function shown in Fig. 5a has its steepest gradient at $\sqrt{2}\Delta$. This ensures heavy weights for direct neighbors (distance Δ), moderate weights for the diagonal neighbors (distance $\sqrt{2}\Delta$) and small weights for all samples at larger distances. Note that the functions can be scaled differently for the two image dimensions or the two velocity components.

Finally, the figure of merit of the regression procedure reads

$$\sum_k w_D(x_k - x, y_k - y)\left[u + \frac{\partial u}{\partial x}(x_k - x) + \frac{\partial u}{\partial y}(y_k - y) - u_k\right]^2 \rightarrow \min \quad \text{and}$$

$$\sum_k w_D(x_k - x, y_k - y)\left[v + \frac{\partial v}{\partial x}(x_k - x) + \frac{\partial v}{\partial y}(y_k - y) - v_k\right]^2 \rightarrow \min, \tag{5}$$

with six parameters (u, $\partial u/\partial x$, $\partial u/\partial y$, v, $\partial v/\partial x$ and $\partial v/\partial y$) to be optimized. Since x and y usually are the coordinates of a certain velocity sample the obtained parameters u and v interfere with the already known velocity at this position. Future developments of the procedure could utilize this redundant information. In the present study only the original velocity estimates are used, which are complemented by the four gradients obtained from the regression.

2.6

Gradients Correction

In principle, the above weighted numerical differentiation can be used to calculate a densely sampled field of velocity gradients. In an optional processing step that has not been implemented in the present study, the obtained gradients can be validated or even corrected using basic fluid flow equations, such as the continuity equation (Tokumaru and Dimotakis, 1995; Okuno et al. , 2000; Nobach and Tropea, 2004, Ruhnau et al. , 2005).

2.7

Velocity Interpolation

Since the redistribution of velocity maps from an unstructured grid to a regular one is common in CFD, this task has often been investigated and several solutions have been developed and reviewed (Imaichi and Ohmi, 1983; Agui and Jimenez, 1987; Jimenez and Agui, 1987; Robinson and Rockwell, 1993; Spedding and Rignot, 1993; Cohn and Koochesfahani, 2000; Lourenco and Krothapalli, 2000; Labonté, 2001; David et al. , 2002).

In the present study, a Gaussian weighted averaging has been used with weights w_I being functions of the distance between the given velocity sample points ($x_k;y_k$) and the points to be interpolated ($x;y$).
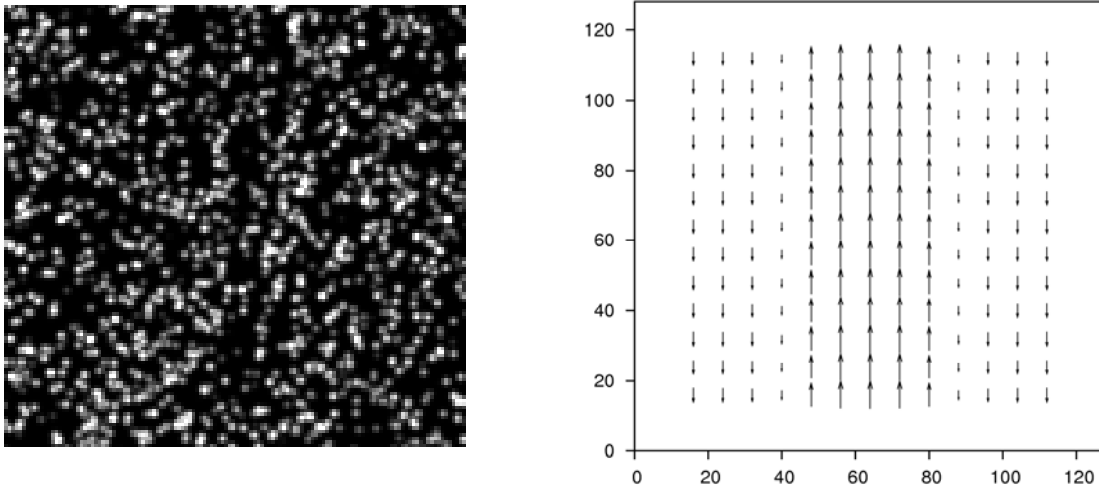
Fig. 6: Test image (128×128 pixel) and vector map of the simulated velocity field

$$u(x;y) = \frac{\sum_k w_I(x - x_k, y - y_k)\left[u_k + \left(\frac{\partial u}{\partial x}\right)_k (x - x_k) + \left(\frac{\partial u}{\partial y}\right)_k (y - y_k)\right]}{\sum_k w_I(x - x_k, y - y_k)} \quad \text{and}$$

$$v(x;y) = \frac{\sum_k w_I(x - x_k, y - y_k)\left[v_k + \left(\frac{\partial v}{\partial x}\right)_k (x - x_k) + \left(\frac{\partial v}{\partial y}\right)_k (y - y_k)\right]}{\sum_k w_I(x - x_k, y - y_k)} \tag{6}$$

The local velocities around the given velocity sample points are found with respect to the previously calculated velocities u_k and v_k and velocity gradients $(\partial u/\partial x)_k$, $(\partial u/\partial y)_k$, $(\partial v/\partial x)_k$ and $(\partial v/\partial y)_k$ at these positions. The optimal width of the weighting function again depends on the chosen density of velocity samples. An optimal interpolation is supposed for the steepest gradient of the weighting function in the middle between directly neighboring velocity samples. Fig. 5b shows the appropriate weighting function for a given distance Δ between the interrogation areas with the steepest gradient at $\Delta/2$.

2.8

Reconstruction on a Given Grid

In principle, the above velocity interpolation method can also be used for the reconstruction of the velocity values on an arbitrary grid. Since the velocity correction loop operates on the pixel-wise sampled hypothetical velocity field, velocity data can be computed directly only if the final grid of the vector map is aligned with the pixel center positions. Assuming an even number of pixels in each dimension of the interrogation area and the coordinate origins at the lower-left corner of the lower-left pixel, the grid points lie exactly between the pixels. Therefore, a reconstruction of the velocity data on the given grid is necessary.

Since the velocity field is sampled at each pixel, the choice of the interpolation scheme is not crucial here. So a simple bi-linear interpolation has been used to derive the velocity values at the final grid of the vector map instead of the more accurate Whittaker reconstruction (Whittaker, 1929), which, unfortunately, is computationally costly.

3

Performance Tests

To demonstrate the capabilities of the full-field correlation-based image processing, synthetic PIV images have been processed. The images of 128×128 pixel size contain approximately 1500 particles, which have varying intensity and a particle image diameter of 3.0 pixels. Fig. 6 shows one of the two images and the simulated displacement field. It is a non-diverging jet flow with two superimposed sigmoidal functions that yield locally different gradients $\partial v/\partial x$.

For comparison, an iterative first-order window deformation algorithm based on numerical differentiation and an iterative algorithm that optimizes the window deformation directly from the image content (Nobach and Tropea, 2005) have been implemented. For better compatibility, the two alternative procedures use the same image interpolation and weighting techniques as the full-field correlation-based method. The obtained velocity estimates and the deviation from the simulated velocity field are shown in Fig. 7.

The results of the procedure based on numerical differentiation clearly show that this method has limited capabilities to follow local changes of the velocity gradients. While the deviations are small at regions of constant velocity, strong deviations occur at the boundaries of the simulated jet. The displacement estimates and the orientation of the deviations indicate a low-pass character of the method. This is obvious, since the velocity gradients are obtained from the difference of neighboring velocity estimates.

Better results could be expected for the method that derives the gradient information directly from the image content. The window offset and deformation are iteratively optimized until the correlation peak is maximized. This allows a comparable spatial resolution for both the velocity and velocity gradient information (Tropea and Nobach, 2005), which leads to a better ability to follow highly dynamic changes of the gradients. Indeed, the results of this procedure in Fig. 7 indicate slightly smaller deviations for this method. However, this algorithm could not derive reliable results at all grid points. Especially in the interesting region of the strong gradient changes, this algorithm is not robust enough to compute reliable results.

Much better results can be obtained with the new processing method. The full-field correlation-based image processing algorithm is not restricted to certain interrogation areas and window deformations. Therefore, reliable velocity and velocity gradient estimates can be obtained even in regions of strong changes of both the fluid velocity and its gradients. The obtained deviations from the simulated flow field are much smaller than for the other algorithms. Furthermore, due to the full-field description of the hypothetical velocity field, the estimates are always valid at all grid points.

4

Summary

A new PIV processing algorithm has been introduced that utilizes a densely sampled, hypothetical velocity field. Based on image correlation, the velocity field is optimized iteratively by correcting residual displacements. The algorithm combines the advantages of the full-field description, which are known for optical flow methods, with the robustness of image correlation. The obtained results of the new procedure on synthetic test images show the excellent characteristics of this procedure. Especially for steep changes of velocity and velocity gradients, this method yields accurate and robust results at a high spatial resolution. Further improvements can be achieved with optimized, optional processing steps, such as validation or physics-based correction of the calculated gradient field. A similar algorithm has been used to process the data for the PIV challenge 2005.

Acknowledgement

References

Agui JC and Jimenez J (1987) On the performance of particle tracking. Journal of Fluid Mechanics, 185, 447–468

Cohn RK and Koochesfahani MM (2000) The accuracy of remapping irregularly spaced velocity data onto a regular grid and the computation of vorticity. Experiments in Fluids, 29, S61–S69

David L, Esnault A and Calluaud D (2002) Comparison of interpolation for 2D and 3D velocimetry. Proc. 11th Int. Symp. on Appl. of Laser Techn. to Fluid Mech., Lisbon, Portugal

Fincham A and Delerce G (2000) Advanced optimization of correlation imaging velocimetry algorithms. Experiments in Fluids, 29, S13–S22

Gui L and Wereley ST (2002) A correlation-based continuous window-shift technique to reduce the peak-locking effect in digital PIV image evaluation, Experiments in Fluids, 32, 506–517

Hart DP (2002) PIV Processing Using Multidimensional Correlation. 10th Int. Symp. on Flow Visualization, August 26-29, 2002, Kyoto, Japan, F0374

Huang OTHT, Fiedler HE and Wang JJ (1995) Limitation and Improvement of PIV: Part II: Particle image distortions, a novel technique. Experiments in Fluids, 15, 263–273

Imaichi K and Ohmi K (1983) Numerical processing of flow visualization pictures. Measurement of two dimensional vortex flow. Journal of Fluid Mechanics, 86, 283–311.

Jambunathan K, Ju XY, Dobbins BN and Ashforth-Frost (1995) An improved cross correlation technique for particle image velocimetry. Meas. Sci. Technol., 6, 507–514

Jimenez J and Agui JC (1987) Approximate reconstruction of randomly sampled signals. Signal Proc., 12, 153–168

Labonté G (2001) Neural network reconstruction of fluid flows from tracer-particle displacements. Experiments in Fluids, 30, 399–499

Lecordier B (1997) Etude de l'interaction de la propagation d'une flamme premelangee avec le champ aerodynamique, par association de la tomographie laser et de la velocimetrie par images de particules. PhD Thesis, l'Universite de Rouen, France

Lindken R, Poelma C, Westerweel J (2003) Compensation for spatial effects for non-uniform seeding in PIV interrogation by signal relocation. 5th Int. Symp. on Particle Image Velocimetry, Busan, Korea, September 22-24, 2003, PIV03, Paper 3302

Lourenco L and Krothapalli A (2000) True resolution PIV: a mesh-free second order accurate algorithm. Proc. 10th Int. Symp. on Appl. of Laser Techn. to Fluid Mech., Lisbon, Portugal

Mayer S (2002) A generalized processing technique in digital particle image velocimetry with direct estimation of velocity gradients. Experiments in Fluids, 33, 443–457

Nobach H (2004) Accuracy of sub-pixel interpolation in PIV and PTV image processing. Technical report, Technische Universität Darmstadt, Fachbereich Maschinenbau, Fachgebiet Strömungslehre und Aerodynamik, Report No. 001/2004

Nobach H and Tropea C (2004) Anwendung von Low Dimensional Models in der Particle Image Velocimetry. Tagungsband 12. Fachtagung "Lasermethoden in der Strömungsmesstechnik", 7.-9. Sept. 2004, Karlsruhe, Germany

Nobach H and Tropea C (2005) Improvements to PIV image analysis by recognizing the velocity gradients. Experiments in Fluids

Nobach H, Damaschke N and Tropea C (2005) High-precision sub-pixel interpolation in particle image velocimetry image processing. Experiments in Fluids.

Nobach H and Honkanen M. (2005) Two-dimensional Gaussian regression for sub-pixel displacement estimation in particle image velocimetry or particle position estimation in particle tracking velocimetry. Experiments in Fluids, 38, 511–515

Nogueira J, Lecuona A and Rodriguez PA (1999) Local field correction PIV: on the increase of accuracy of digital PIV systems. Experiments in Fluids, 27, 107–116

Nogueira J, Lecuona A and Rodríguez PA (2001) Identification of a new source of peak locking, analysis and its removal in conventional and super-resolution PIV techniques. Experiments in Fluids, 30, 309–316

Okuno T, Sugii Y and Nishio S (2000) Image measurement of flow field using physics-based dynamic model. Meas. Sci. Technol. 11, 667–676

Robinson O and Rockwell D (1993) Construction of 3D images of flow structures via particle tracking techniques. Experiments in Fluids, 14, 257–270

Ronneberger O, Raffel M and Kompenhans J (1998) Advanced Evaluation Algorithms for Standard and Dual Plane Particle Image Velocimetry. Proc. 9th Int. Symp. on Appl. of Laser Techn. to Fluid Mech., Lisbon, Portugal

Ruhnau P, Kohlberger T, Schnörr C and Nobach H (2005) Variational optical flow estimation for particle image velocimetry. Experiments in Fluids 38, 21–32

Scarano F (2002) Iterative image deformation methods in PIV. Meas. Sci. Texchnol. 13, R1–R19

Scarano F and Riethmuller ML (2000) Advances in iterative multigrid PIV image processing. Experiments in Fluids, 29, S51–S60

Spedding GR and Rignot EJM (1993) Performance analysis and application of grid interpolation techniques for fluid flows. Experiments in Fluids, 15, 417–430

Tokumaru OT and Dimotakis PE (1995) Image correlation velocimetry. Experiments in Fluids, 19, 1–15

Whittaker JM (1929) The Fourier theory of the cardinal functions. Proc. - R. Soc. Edinburgh Sect. A Math., 1, 169–176

Willert CE (2000) Evaluation of digital PIV recordings. In: Application of Particle Image Velocimetry – Theory and Practice, Course Notes, March 6–10 2000, DLR Göttingen, Germany

Young CN, Johnson DA and Weckman EJ (2002) A model based validation strategy for cross correlation PIV. Proc. 11th Int. Symp. on Appl. of Laser Techn. to Fluid Mech., Lisbon, Portugal, paper 6.1

Young CN, Johnson DA and Weckman EJ (2004) A method to anchor displacement vectors to reduce uncertainty and improve particle image velocimetry results. Meas. Sci. Technol., 15, 9–20
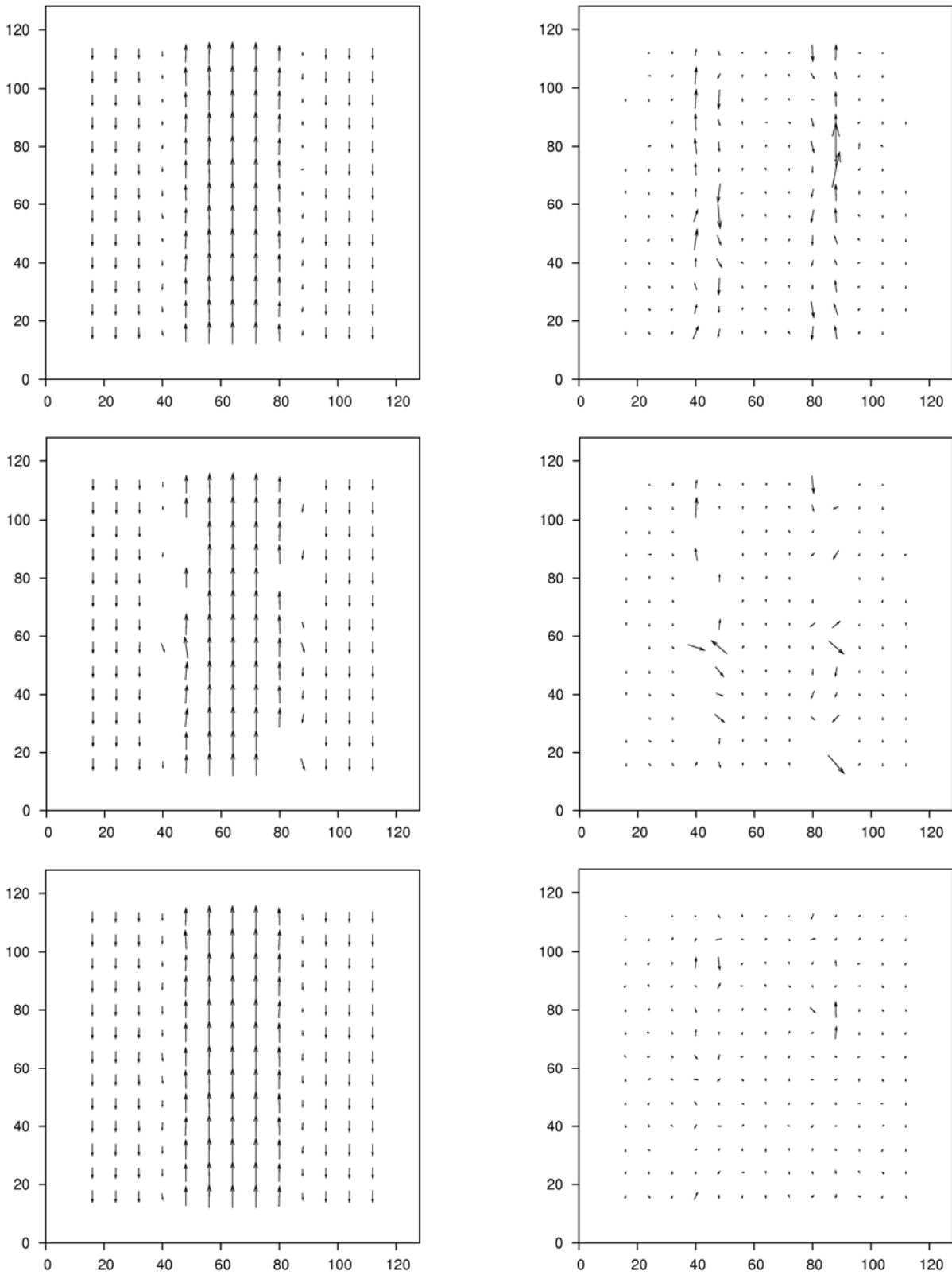
Fig. 7: Results of the test image processing: Displacement estimates (left) and deviation from the simulated vector field (right, magnified by 5); numerical differentiation (top), direct optimization of the window deformation (middle) and full-field, correlation based image processing (bottom)